J. Fluid Mech. (2019), *vol.* 877, *pp.* 471–494. © Cambridge University Press 2019
doi:10.1017/jfm.2019.599

Hypersonic compression corner flow with large separated regions

Sudhir L. Gai[1] **and Amna Khraibut**[1,†]

[1]University of New South Wales, Canberra, 2612, Australia

(Received 6 December 2018; revised 22 July 2019; accepted 22 July 2019;
first published online 27 August 2019)

The structure of large-scale hypersonic boundary layer separation and reattachment is studied numerically using a flat plate/compression corner geometry. Apart from verifying the large scale separation characteristics in hypersonic flow, a detailed discussion of secondary separation and fragmentation into multiple vortices embedded within the main recirculation region is presented. The unique relation between the second minimum in shear stress and the scaled angle is highlighted in the context of the reverse flow singularity of Smith (*Proc. R. Soc. Lond.* A, vol. A420, 1988, pp. 21–52) and it appears that for a small wall temperature ratio, such a singularity is unlikely. It is shown that the size of the separation can be estimated in terms of Burggraf's expression based on asymptotic theory.

Key words: high-speed flow, boundary layer separation, compressible boundary layers

1. Introduction

In recent years, in several investigations of supersonic and hypersonic shock wave/boundary layer interactions (SBLI) involving large separated regions, numerical studies have shown multiple vortex structures/eddies embedded in the main separation bubble (Smith & Khorrami 1991; Korolev, Gajjar & Ruban 2002; Neiland, Sokolov & Shvedchenko 2008; Shvedchenko 2009). The critical parameter governing the origin and existence of these eddies seems to be the geometric angle $\alpha^* = O(Re^{-1/4})$, which represents the strength of perturbation to the boundary layer such as a shock wave inducing separation at a compression corner or a shock wave from a wedge incident on a boundary layer growing over a surface such as a flat plate beneath the wedge. It must be emphasised that the existence of these eddies is based mainly on numerical simulations of mainly two-dimensional flows involving large separated regions.

In terms of supersonic triple-deck theory, a separation bubble is said to be small when the length of the bubble is $O(lRe^{-3/8})$ or less and both separation and reattachment are contained within it. Here, l is the characteristic length such as the distance from the leading edge to the compression corner or the point of incidence of an incident shock on a boundary layer over a flat plate; Re is a characteristic Reynolds number based on l and the free-stream/boundary layer edge conditions. If the bubble length is greater than or equal to $O(l)$, separation is said to be large, in

†Email address for correspondence: amnakhraibut80@gmail.com

https://doi.org/10.1017/jfm.2019.599 Published online by Cambridge University Press

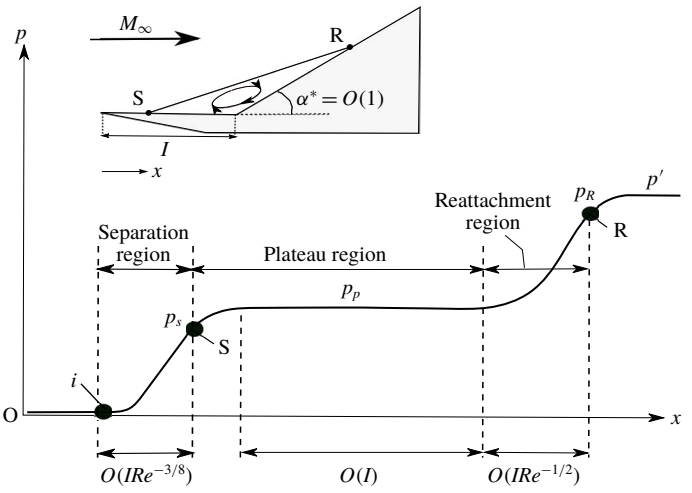


FIGURE 1. Typical pressure distribution in a large separated region in a supersonic flow ($M_\infty < 5$).

which case separation and reattachment processes are no longer interconnected but separated by a large region of nearly constant pressure (Burggraf 1975). Thus, a large separation bubble characteristically consists of three distinct but contiguous regions (figure 1) – an initial rise up to separation, with length $O(lRe^{-3/8})$, a large plateau region of constant pressure $O(l)$, which is followed by the reattachment region of $O(lRe^{-1/2})$ in extent that is largely an inviscid process (Burggraf 1975; Daniels 1979).

With hypersonic flows, there is an additional parameter σ which includes the effects of both the hypersonic viscous interaction parameter and wall cooling; σ as defined in Brown, Cheng & Lee (1990) is the ratio of the wall temperature and the critical wall temperature, as in Cheng (1993).

Referring to figure 1, the point wherein separation just appears (S), the so-called incipient separation, has a scaled angle $\alpha_{in} = 1.57$ where α is defined as in (1.1), and it can be completely described in terms of triple-deck theory. It is also consistent with Chapmans free-interaction theory (Chapman, Kuehn & Larson 1958). Burggraf (1975), Korolev *et al.* (2002) and Neiland *et al.* (2008) have shown that large separated regions can be analysed by extending the triple-deck approach.

A second characteristic feature of a large separated region is the presence of a second minimum (figure 2) in the shear stress distribution curve immediately before reattachment. It is usually larger and steeper than the first in magnitude. The significance of this second minimum has been discussed previously by Smith (1988), Smith & Khorrami (1991) and Korolev *et al.* (2002). Its dependence on the scaled angle α has been the subject of much discussion and analysis by Smith (1988), Smith & Khorrami (1991), Korolev *et al.* (2002) and Neiland *et al.* (2008).

A third characteristic of large separated flows in both supersonic and hypersonic SBLI that has drawn the attention of researchers in recent years is the existence of secondary and even tertiary eddies embedded within the main recirculation region of the separation bubble. Discussion of such a feature in two-dimensional separated flows has been presented by Smith & Khorrami (1991) and Korolev *et al.* (2002). Further, dependence of such multiple eddies on wall temperature and Reynolds number has recently been investigated by Neiland *et al.* (2008) and Shvedchenko

https://doi.org/10.1017/jfm.2019.599 Published online by Cambridge University Press

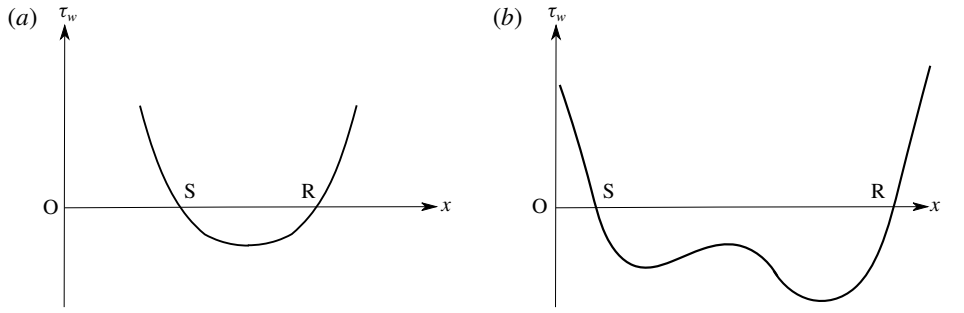


FIGURE 2. Shear stress distribution in a small and large separation. (*a*) Small separation; (*b*) large separation.

(2009), Egorov, Neiland & Shvedchenko (2011) and Khraibut *et al.* (2017) in the context of hypersonic SBLI.

In considering large separated regions in supersonic and hypersonic flows, a measure of the extent of separation can be given in terms of the scaled angle α as defined in Stewartson (1970)

$$\alpha = \frac{\alpha^* Re^{1/4}}{C^{1/4}\lambda^{1/2}\beta^{1/2}}, \tag{1.1}$$

where α^* is typically a geometric angle in a compression corner or a corresponding semi-angle of a wedge generating a shock wave incident on a boundary layer developed on a flat plate and provoking separation. Here, Re is a characteristic Reynolds number, C is the Chapman–Rubesin parameter, λ is a shear constant (0.332 in the case of a Blasius boundary layer) and $\beta = (M^2 - 1)^{1/2}$. For hypersonic flows $\beta \approx M$.

A comment needs to be made here regarding the definition of the scaled angle α. Different researchers have used different definitions without providing reasons. For example, Neiland *et al.* (2008) and Shvedchenko (2009) have used $\alpha = \alpha^* Re^{1/4}$, which ignores the Mach number effect as well as the shear constant and the Chapman–Rubesin parameter of the boundary layer prior to separation. Subsequently, Egorov *et al.* (2011) used $\alpha = \alpha^* Re^{1/4}/\beta^{1/2}$, which includes the Mach number but no shear constant and Chapman–Rubesin parameter. Herein, we have used the definition as given in Stewartson (1970) and Rizzetta, Burggraf & Jenson (1978), which is consistent with the triple-deck assumptions.

Studies by Smith & Khorrami (1991), Korolev *et al.* (2002) and Shvedchenko (2009) show that a secondary eddy begins to appear in the recirculating region when $4 \leqslant \alpha \leqslant 5$. A steady secondary eddy persists up to $\alpha \leqslant 6$. Beyond this, further fragmentation leads to multiple eddies.

Some remarks regarding the existence of secondary eddies in axisymmetric flows may be relevant here. Although substantial computational and experimental effort has been put into investigating double-cone and hollow cylinder/flare hypersonic SBLI (see for example, Holden *et al.* 2003 and Nompelis, Candler & Holden 2003), involving large separations, there has not been much mention or sufficient discussion of secondary vortices in these flows. Recently, Tumuklu, Levin & Theofilis (2018) in their discussion of Reynolds number effects on separation over a double-cone flow, have reported the presence of secondary vortex upstream of the junction of the two cones at Reynolds numbers greater than 2.8×10^5. The corresponding scaled

https://doi.org/10.1017/jfm.2019.599 Published online by Cambridge University Press

angle α in this case was 14.3. At a Reynolds number of 9.3×10^4, corresponding to $\alpha = 11$, they observed a large separation but no secondary vortex. These values are considerably larger than in the case of a two-dimensional compression corner for steady secondary eddies to exist. Benay *et al.* (2006) conducted a numerical and experimental investigation of a hollow cylinder/flare in a Mach 5 flow. The conical flare angle was 15°. The Reynolds number range was 3.8×10^5 to 8.3×10^5 when the flow remained laminar. The Reynolds number was based on free-stream conditions and the length L, the distance from the leading edge of the cylinder to the cylinder/flare junction. The wall to stagnation temperature ratio was 0.6.

The agreement between experiments and numerical data was good within the laminar range. The authors' numerical data showed that a secondary eddy, located slightly upstream of the cylinder/flare junction, first appeared at $Re_L = 8.3 \times 10^5$ with a scaled angle $\alpha = 6.1$. Again, this is higher than the 4–5 predicted by Smith & Khorrami (1991) and Korolev *et al.* (2002). Benay *et al.* (2006) observed multiple eddies at higher Reynolds numbers of 16×10^5 and 22.4×10^5 corresponding to $\alpha = 7.23$ and 7.86, respectively. They, however, inferred that the secondary eddies are 'non-physical' based on their laser Doppler velocimetry (LDV) measurements. They further conjectured that the secondary eddies are a consequence of forcing a two-dimensional laminar Navier–Stokes solution on to an axisymmetric flow and that implementing a three-dimensional solution would result in the formation of Görtler vortices instead, eventually leading to transition.

Gittler & Kluwick (1987) have analysed laminar separation on an axisymmetric hollow cylinder/flare in an adiabatic wall supersonic flow based on the triple-deck theory. According to these results, large separation (as evidenced by a distinct plateau in the pressure distribution curve) does not occur before $\alpha \approx 9$. Also, from their shear stress data, it would appear that incipient separation occurs when $3 \leqslant \alpha_{in} \leqslant 4$, which is more than double the two-dimensional incipient separation value of $\alpha_{in} \approx 1.57$ as found by Rizzetta *et al.* (1978). It would, therefore, appear that secondary separation in axisymmetric flow appears at substantially higher values of α compared to the two-dimensional flow.

2. The compression corner geometry

This is a much studied SBLI configuration at supersonic and hypersonic speeds both experimentally (for example, Holden 1966; Lewis, Kubota & Lees 1968; Délery & Marvin 1986; Mallinson, Gai & Mudford 1997), and numerically (Hung & MacCormack 1976; Rudy *et al.* 1989; Olejniczak & Candler 1998; Deepak, Gai & Neely 2013). These studies present an exhaustive discussion and analyses of both experimental as well as numerical simulations, which have shown agreement of varying degrees with one another. None of these studies, however, discusses details of the internal structure of the separation bubble such as the presence of secondary vortices and their development mentioned earlier in the Introduction, although some of the above studies did involve large separations. It is only in recent years that existence of secondary vortices in large separated regions induced at a compression corner have been discussed by Neiland *et al.* (2008) and Shvedchenko (2009), Egorov *et al.* (2011). These authors have shown that, depending on the magnitude of the scaled angle α, the separated region might develop secondary separation and as a consequence, transverse gradients which ultimately lead to instability, fragmentation and three-dimensional flow.

In the present paper, we have considered one of the experimental flow conditions and the model used in Mallinson (1994), and performed an extensive numerical

https://doi.org/10.1017/jfm.2019.599 Published online by Cambridge University Press

M_∞	Re_∞ (1 m^{-1})	U_∞ (m s^{-1})	p_∞ (Pa)	T_∞ (K)	ρ_∞ (Kg m^{-3})
9.1	32.2×10^5	2280	730	160	0.016

TABLE 1. Free-stream conditions: condition G in Mallinson (1994).

investigation of separated flows ranging from incipient to large separated flows with particular emphasis on the secondary vortices/eddies. The model used was a compression corner consisting of a flat plate 85 mm in length and a ramp plate 95 mm long attached at the end of the flat plate. The ramp plate was adjustable to give a range of corner deflection angles up to 24°. The model span was 180 mm so that the aspect ratio (span/flat plate length) was 2.1. Full geometrical and installation details are given in Mallinson (1994).

The flow conditions used in this study are given in table 1, where M, T, p, ρ and Re are the Mach number, temperature, pressure, density and Reynolds number, respectively, and subscript ∞ denotes the free-stream conditions. The flow was laminar throughout and the wall-to-stagnation temperature ratio was 0.125. The value of the hypersonic viscous interaction parameter, based on free-stream and corner conditions, was 1.24. For the present numerical study, six flow deflection angles – 10°, 12°, 14°, 16°, 18° and 24°, were used. These yield near incipient to large separated flows. The scaled angles corresponding to these geometric angles were 2.48, 2.98, 3.47, 3.97, 4.47 and 5.95, respectively.

Mallinson (1994) used two more flow conditions in their experiments, apart from that mentioned above. These, however, were lower Reynolds number and Mach number flow conditions. The unit Reynolds numbers were nearly an order of magnitude lower and the Mach number was 7.5. As the main objective of the present investigation concerns the existence of and properties of secondary separation in a large separated flow, and comparison of the results with the asymptotic high Reynolds number theory, the highest Reynolds number and Mach number condition has been used for the present study. This flow condition has been used along with a higher specific enthalpy and lower Reynolds number and Mach number flow condition by Deepak *et al.* (2013) in another numerical investigation to study the effect of real gas models on separated flows.

3. Numerical procedure

3.1. *Governing equations*

In general, the hypersonic SBLI in the continuum flows is accurately described by the compressible Navier–Stokes (N-S) flow equations. The generalised three-dimensional N-S equations for a perfect gas expressed in vector notation are

$$\frac{\partial \boldsymbol{U}}{\partial t} + \frac{\partial \boldsymbol{F}}{\partial x} + \frac{\partial \boldsymbol{G}}{\partial y} + \frac{\partial \boldsymbol{H}}{\partial z} = 0, \tag{3.1}$$

where the vector

$$\boldsymbol{U} = \{\rho, \rho u, \rho v, \rho w, E\}, \tag{3.2}$$

where $\boldsymbol{F}$, $\boldsymbol{G}$ and $\boldsymbol{H}$ are the flux vectors in Cartesian coordinates x (streamwise direction), y (vertical direction) and z (normal to x–y plane), respectively. In the

https://doi.org/10.1017/jfm.2019.599 Published online by Cambridge University Press

expression of $\boldsymbol{U}$ (equation (3.2)), ρ, T, p and E denote the density, temperature, pressure and total energy per unit volume, respectively. The pressure is calculated using

$$p = (\gamma - 1)\rho\epsilon, \tag{3.3}$$

where

$$\epsilon = E/\rho - 0.5(u^2 + v^2 + w^2), \tag{3.4}$$

and γ is the ratio of specific heats c_p/c_v.

$$\boldsymbol{F} = \begin{bmatrix} \rho u \\ \rho u^2 + p \\ \rho v u \\ \rho w u \\ (E+p)u \end{bmatrix} + \begin{bmatrix} 0 \\ \tau_{xx} \\ \tau_{yx} \\ \tau_{zx} \\ \tau_{xx}u + \tau_{yx}v + \tau_{zx}w - k\dfrac{\partial T}{\partial x} \end{bmatrix}, \tag{3.5}$$

$$\boldsymbol{G} = \begin{bmatrix} \rho v \\ \rho u v \\ \rho v^2 + p \\ \rho w v \\ (E+p)v \end{bmatrix} + \begin{bmatrix} 0 \\ \tau_{xy} \\ \tau_{yy} \\ \tau_{zy} \\ \tau_{xy}u + \tau_{yy}v + \tau_{zy}w - k\dfrac{\partial T}{\partial y} \end{bmatrix}, \tag{3.6}$$

$$\boldsymbol{H} = \begin{bmatrix} \rho w \\ \rho u w \\ \rho v w \\ \rho w^2 + p \\ (E+p)w \end{bmatrix} + \begin{bmatrix} 0 \\ \tau_{xy} \\ \tau_{yy} \\ \tau_{zy} \\ \tau_{xz}u + \tau_{yz}v + \tau_{zz}w - k\dfrac{\partial T}{\partial z} \end{bmatrix}, \tag{3.7}$$

and the shear stress tensor is estimated using the Chapman–Enskog approximation as

$$\tau_{xx} = -\lambda\left(\frac{\partial u}{\partial x} + \frac{\partial v}{\partial y} + \frac{\partial w}{\partial z}\right) - 2\mu\frac{\partial u}{\partial x}, \tag{3.8}$$

$$\tau_{yy} = -\lambda\left(\frac{\partial u}{\partial x} + \frac{\partial v}{\partial y} + \frac{\partial w}{\partial z}\right) - 2\mu\frac{\partial v}{\partial y}, \tag{3.9}$$

$$\tau_{zz} = -\lambda\left(\frac{\partial u}{\partial x} + \frac{\partial v}{\partial y} + \frac{\partial w}{\partial z}\right) - 2\mu\frac{\partial w}{\partial z}, \tag{3.10}$$

$$\tau_{xy} = \tau_{yx} = -\mu\left(\frac{\partial u}{\partial x} + \frac{\partial v}{\partial x}\right), \tag{3.11}$$

$$\tau_{xz} = \tau_{zx} = -\mu\left(\frac{\partial u}{\partial z} + \frac{\partial x}{\partial x}\right), \tag{3.12}$$

$$\tau_{yz} = \tau_{zy} = -\mu\left(\frac{\partial v}{\partial z} + \frac{\partial w}{\partial y}\right). \tag{3.13}$$

Here, μ and λ are the first and second coefficients of viscosity, respectively, whereas k is the thermal conductivity.

The flux terms (equations (3.5)–(3.7)) can be conveniently decomposed into inviscid and viscous terms such that

$$\boldsymbol{A} = \boldsymbol{A}_i + \boldsymbol{A}_v, \tag{3.14}$$

https://doi.org/10.1017/jfm.2019.599 Published online by Cambridge University Press

where A is generic for any of the $\boldsymbol{F}$, $\boldsymbol{G}$ and $\boldsymbol{H}$ vectors and subscripts 'i' and 'v' denote inviscid and viscous components, respectively. It should be pointed out that the first rows in (3.5)–(3.7) refer to the conservation mass terms, rows 2–4 are the conservation of momentum terms and row 5 terms are associated with the conservation of energy. The τ terms in (3.7) and (3.13) moreover assume a homogeneous, isotropic Newtonian fluid and only change with velocity gradients.

3.2. *Description of solver, free-stream conditions and simulations*

Numerical simulations of a compression corner for various deflection angles were carried out using a continuum flow solver US3D. US3D was developed at the University of Minnesota specifically for high-speed flows (Nompelis & Candler 2014; Candler *et al.* 2015). It is capable of carrying out both perfect gas and real gas simulations, and has been validated for a wide range of hypersonic flow problems (Drayna, Nompelis & Candler 2006; Candler, Subbareddy & Brock 2014; MacLean, Holden & Dufrene 2014). The code uses parallel processing to improve computational speed and allows both implicit and explicit time integrations to be conducted.

Representation of the discretised N-S equations expressed in the implicit formulation as well as the resolution of viscous and inviscid terms to obtain a finite volume representation of the N-S equations have been given in Wright, Candler & Bose (1998).

Steady-state solutions in US3D are obtained using the modified Steger–Warming flux vector splitting method (Candler *et al.* 2015), and the Jacobians are evaluated such that the dissipation is low, as typically required in hypersonic simulations (Wright *et al.* 1998; MacCormack 2014). The solver uses the monotonic upstream-centred (MUSCL) scheme of Van Leer (1979) to give second-order spatially accurate solutions. The code permits the use of flux limiters to prevent non-physical solutions from occurring (MacCormack 2014). The default Osher limiter (Nompelis & Candler 2014) is utilised in the present simulations, having good dissipation characteristics.

Data parallel line relaxation (DPLR) which is implemented in US3D is capable of handling stretched cells seen in hypersonic applications, without degrading the method's performance (Wright *et al.* 1998). The DPLR method, however, requires more memory storage compared to other methods, while it is also able to converge at a much faster rate (Wright *et al.* 1998). Implicit time integration is chosen in the study to allow large Courant–Friedrichs–Lewy (CFL) numbers to be used.

Two-dimensional simulations assume a laminar flow given the moderate Reynolds number flow under consideration. They also take the walls to be non-catalytic and impose a no-slip boundary condition on the walls. The operating gas is taken as a 5-species air, and the simulations are based on the perfect gas assumption.

The viscosities are evaluated using Blottner curve fits and Wilke's mixing rule for the mixture (Wilke 1950; Blottner, Johnson & Ellis 1971), while thermal conductivities are calculated using Eucken's correction (Candler *et al.* 2015).

The free-stream conditions used for this compression corner study described in § 2 are based on experimental condition G in Mallinson (1994), Mallinson *et al.* (1997), Olejniczak & Candler (1998) and Deepak *et al.* (2013). Separate grid independence studies were carried out for these flow conditions by Olejniczak & Candler (1998) and Deepak *et al.* (2013) for corner angles $\alpha^* = 10^\circ$ and 18°. For $\alpha^* = 18^\circ$, Olejniczak & Candler (1998) indicated grid independence with 262×10^3 cells. Deepak *et al.* (2013), on the other hand, used a much coarser grid with 60×10^3 cells, using the time accurate code Eilmer3 of Jacobs & Gollan (2010).

https://doi.org/10.1017/jfm.2019.599 Published online by Cambridge University Press

Index (k)	i	j	n (Million)
1	4031	1009	4.1
2	3200	801	2.6
3	1798	450	0.9
4	1194	299	0.36

TABLE 2. Summary of grids used in grid convergence study ($\alpha^* = 18°$).

In the present study, we consider compression angles starting from incipient separation at 10°–18° with 2 degree increments, and finally 24°, which yields a large separation. The grid independence study was carried out for the 18° deflection angle because it yields a sufficiently large separation, and is also sufficient to verify the other cases. The finest grid for this case is therefore used in the simulations of other deflection angles.

Table 2 summarises the grids used in the grid independence study, where cell numbers varied between nearly 360 000 cells in the coarsest grid and 4 million cells in the finest. Index k in the table refers to the grids in a descending order, i being the number of nodes in the streamwise direction and j the number of nodes in the transverse direction, with n is the total number of cells.

3.3. *Convergence study*

Surface data, shear stress, pressure and heat flux are monitored to determine convergence of the solution. This convergence study considers the 18° compression angle, which yields a sufficiently large separated region and can be validated against the experimental data of Mallinson (1994). The shear stress is important because it defines the length of separation as it crosses the zero line from positive to negative at separation and negative to positive at reattachment. The pressure and heat flux, on the other hand, are experimentally measurable quantities in short-duration facilities. The surface parameters are shown on a global scale for grids 1–4 in figures 3–5, where s is the non-dimensional wetted distance s^*/L where L is the length of the flat plate, C_f is the ratio of wall shear stress to dynamic pressure $0.5\rho_\infty \boldsymbol{U}_\infty^2$, C_p is the surface pressure to dynamic pressure ratio and C_h is the heat flux to the quantity $0.5\rho_\infty \boldsymbol{U}_\infty^3$ ratio. It was also noted that all grids reached steady state with a minimum of a five order drop in root mean square (RMS) residuals, and in these figures, the different curves pertain to these steady-state solutions for each grid.

Considering figure 3, which shows the shear stress data, the size of the recirculation region is determined as the shear stress crosses the zero line from positive to negative at separation and from negative to positive at reattachment (see (*a*) and (*b*)). Multiple crossings of the zero line indicate fragmented vortices within the main separation region ((*b*) and (*c*)). During the grid independence study, it was noted that these secondary structures within the primary separation are quite sensitive to first cell height and level of convergence of the solution, and the attainment of a steady state.

Pressure and heat flux data are similarly shown in figures 4 and 5 with the magnified views of the corner flow shown in (*b*) and (*c*) of the figures. We also note changes of pressure and heat flux with grid refinement. It should be noted also that grid 4 used in the present simulations is of the same size as the reported converged grid in Deepak *et al.* (2013) using a time explicit solver ($\approx$ 360 K cells). The present

https://doi.org/10.1017/jfm.2019.599 Published online by Cambridge University Press

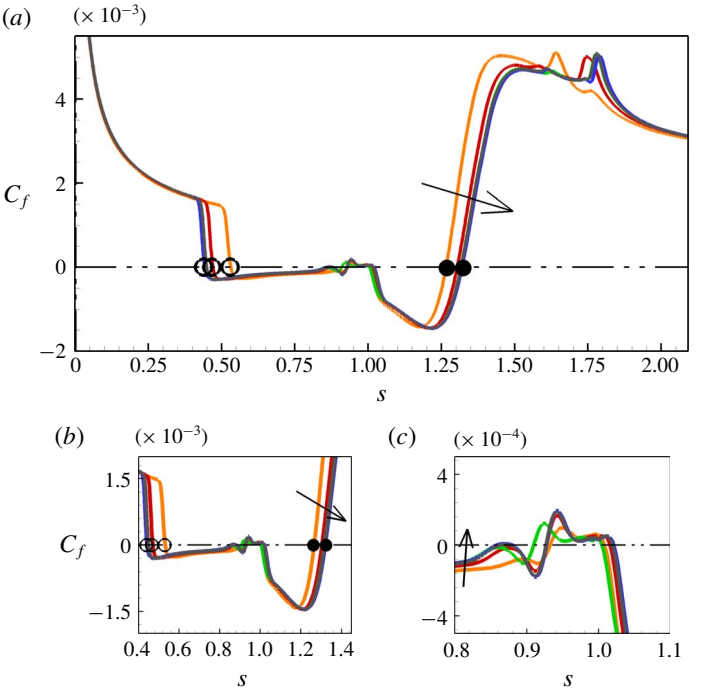


FIGURE 3. (Colour online) Convergence of the shear stress C_f in the $\alpha^* = 18°$ compression corner case. Blue: grid 1; green: grid 2; red: grid 3; orange: grid 4. Open circles: separation; closed circles: reattachment. Arrow points in direction of increased grid refinement. (*a*) Global distribution; (*b*) main separation; (*c*) near the vertex.

simulations show that at least ten times the number of cells in that grid compared to grid 2 (at least 3 millions) were required to reach convergence.

Separation length l_B is a good measure of the quality of the numerical solution as pointed out by Druguet, Candler & Nompelis (2005). Table 3 compares the non-dimensional locations of separation (s_S) and reattachment s_R, and the separation length l_B in the present grid convergence study for all four grids and those for the reported converged grid by Deepak *et al.* (2013). It is seen that the present simulations show an increase of 27.3 % in the separation length l_B, occurring mainly as a result of separation point moving upstream by 37.62 %, and reattachment moving downstream by 5.52 %. The experimental data from Mallinson (1994) indicate that the non-dimensional length of separation for condition G at $\alpha^* = 18°$ is 0.8. The computations, therefore, seem to over-predict the same length by less than 10 %.

3.4. *Grid error analysis*

The mixed-order method is used to carry out a systematic grid error analysis as it deals well with flow discontinuities such as shock waves. The method has been described in detail by Roy (2003) by retaining both first-order and second-order terms in the generalised Richardson extrapolation technique

$$f = f_{exact} + g_1 h + g_2 h^2 + O(h^3), \tag{3.15}$$

https://doi.org/10.1017/jfm.2019.599 Published online by Cambridge University Press

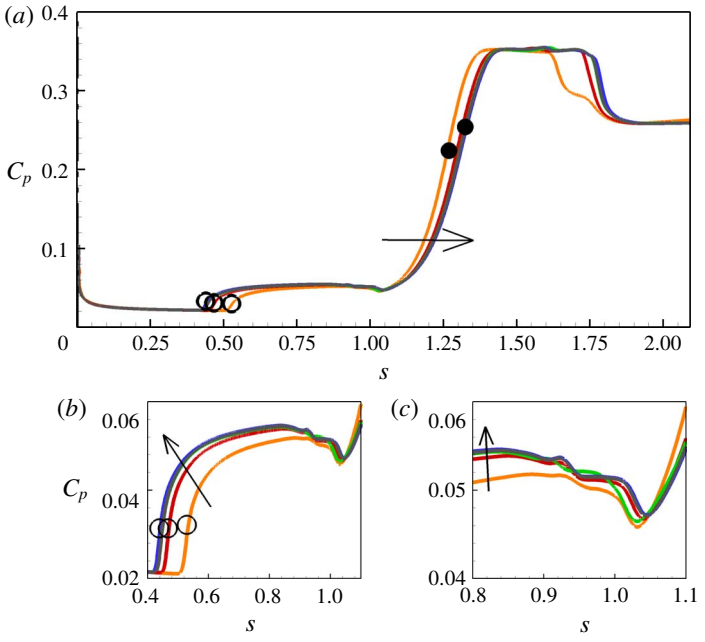


FIGURE 4. (Colour online) Convergence of the surface pressure C_p in the $\alpha^* = 18°$ compression corner case. Blue: grid 1; green: grid 2; red: grid 3; orange: grid 4. Open circles: separation; closed circles: reattachment. Arrow points in direction of increased grid refinement. (*a*) Global distribution; (*b*) main separation; (*c*) near the vertex.

	s_S	s_R	l_B
Grid 1	0.4425	1.32	0.878
Grid 2	0.449	1.317	0.868
Grid 3	0.470	1.304	0.833
Grid 4	0.529	1.277	0.748
Previous numerical	0.609	1.247	0.638
Experimental	0.6	1.4	0.8

TABLE 3. Comparison of separation length with previous numerical study of Deepak *et al.* (2013) and experiments of Mallinson (1994) for a compression angle of $\alpha^* = 18°$.

which requires all grid solutions to be within the asymptotic range of f_{exact} and continuous. Expanding (3.15) to at least three grids yields an exact solution as

$$f_{exact} = f_1 + \frac{\epsilon_{32}(r_{12} - 1) - \epsilon_{21}(r_{12}r_{23}^2 - r_{12} - r_{23} - 1)}{(r_{12} - 1)(r_{23} - 1)(r_{12}r_{23} - 1)}, \tag{3.16}$$

where $\epsilon_{32} = f_3 - f_2$, $\epsilon_{21} = f_2 - f_1$, $r_{12} = h_1/h_2$, $r_{23} = h_2/h_3$.

Here, f_{exact} can be evaluated for any parameter of interest to convergence, which in the case of separated flows are the surface parameter at separation S and reattachment R as

$$|\text{Spatial error}| = 3\left|\frac{f_{1-3} - f_{exact}}{f_{exact}}\right| \times 100, \tag{3.17}$$

https://doi.org/10.1017/jfm.2019.599 Published online by Cambridge University Press

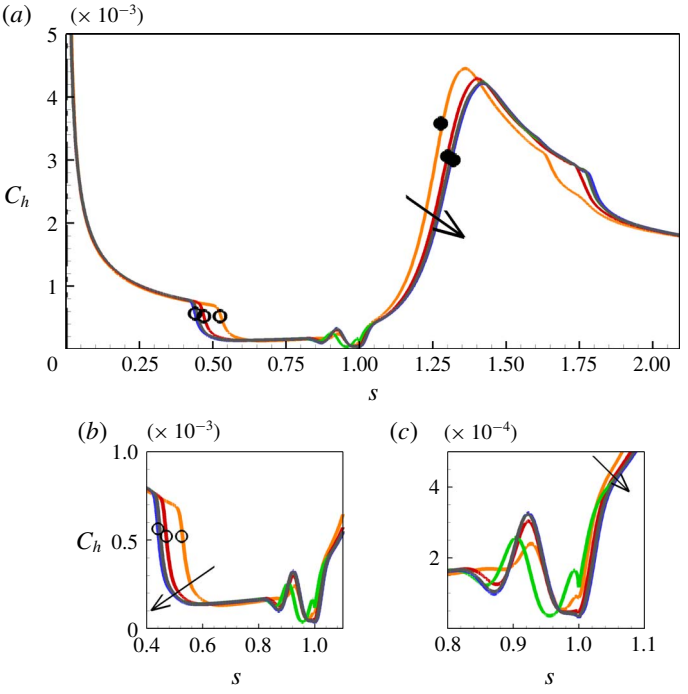


FIGURE 5. (Colour online) Convergence of the heat flux C_h in the $\alpha^* = 18°$ compression corner case. Blue: grid 1; green: grid 2; red: grid 3; orange: grid 4. Open circles: separation; closed circles: reattachment. Arrow points in direction of increased grid refinement. (*a*) Global distribution; (*b*) main separation; (*c*) near the vertex.

where the number three seen in the equation is a safety factor to give a conservative estimate of the error.

Figure 6 shows changes of the spatial error with grid refinement in terms of the number of cells used in each grid. The blue square symbols denote the location of separation, while the closed red circles denote reattachment. In the figure, the coarsest grid 4 yielded the highest error values at separation (≈60 %) and reattachment (≈10 %). This shows that the location of separation s_S is more sensitive to grid refinement that the location of reattachment s_R. It can be noted further that grid 2 yields spatial error values within 6 % of the exact locations of separation and reattachment. Discussion of results to follow is based on the finest grid 1 solutions which show separation to be within 2 % of the exact value with a safety factor of three. This grid size is therefore used for other compression angles.

4. Results and discussion

4.1. *General flow characteristics*

Figures 7 and 8 show results for non-dimensional surface pressure C_p and shear stress C_f, respectively, for these deflection angles.

The pressure curves (figure 7) illustrate all the major features of moderate to large separated regions as delineated in figure 1. The initial rise in pressure up to separation (open circles) is followed by a distinct plateau after approximately 12°, after which it grows with the increase in the corner angle. At the largest corner angle of 24°,

https://doi.org/10.1017/jfm.2019.599 Published online by Cambridge University Press

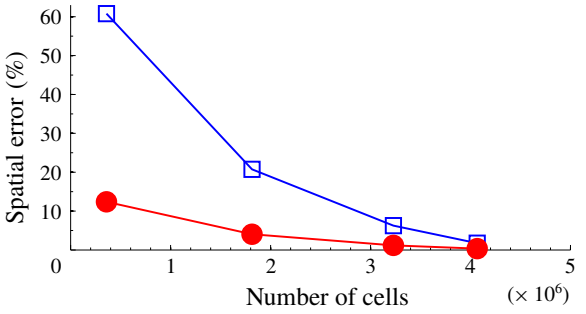


FIGURE 6. (Colour online) Changes in spatial error with grid refinement in terms of the number of cells. Blue squares: separation; red circles: reattachment.

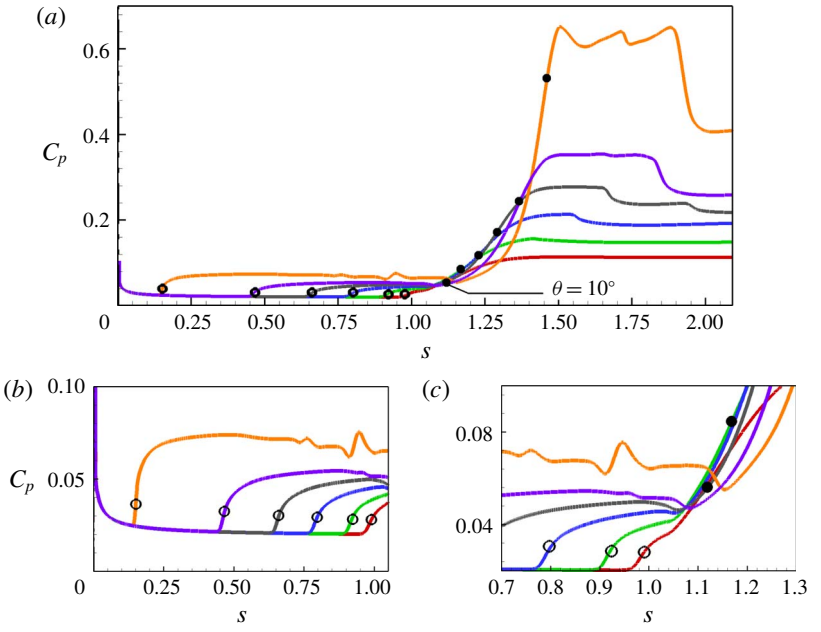


FIGURE 7. (Colour online) Variation of pressure with different deflection angles. Red: 10°; green: 12°; blue: 14°; grey: 16°; purple: 18°; orange: 24°. Open circles: separation; closed circles: reattachment. (*a*) Global distribution; (*b*) near the leading edge; (*c*) near the corner.

we note three distinct peaks after reattachment. These peaks are the result of multiple vortices, as will be shown later. The inset in the figure shows the pressures in the vicinity of the corner. Again, we notice some significant fluctuations with the 24° angle. We also note that as the corner is approached, there is a local drop in pressures, which is indicative of secondary vortices (see Smith & Khorrami 1991; Korolev *et al.* 2002; Egorov *et al.* 2011).

This dip in pressure is particularly noticeable for angles 16°, 18° and 24°, corresponding to scaled angles of 3.97, 4.47 and 5.95, respectively. This is consistent with the previous observations of Smith & Khorrami (1991), Korolev *et al.* (2002) and Shvedchenko (2009) that steady secondary separation appears at $3 \leqslant \alpha \leqslant 4$ and instability in secondary separation and fragmentation occurs when $\alpha \geqslant 6$.

https://doi.org/10.1017/jfm.2019.599 Published online by Cambridge University Press

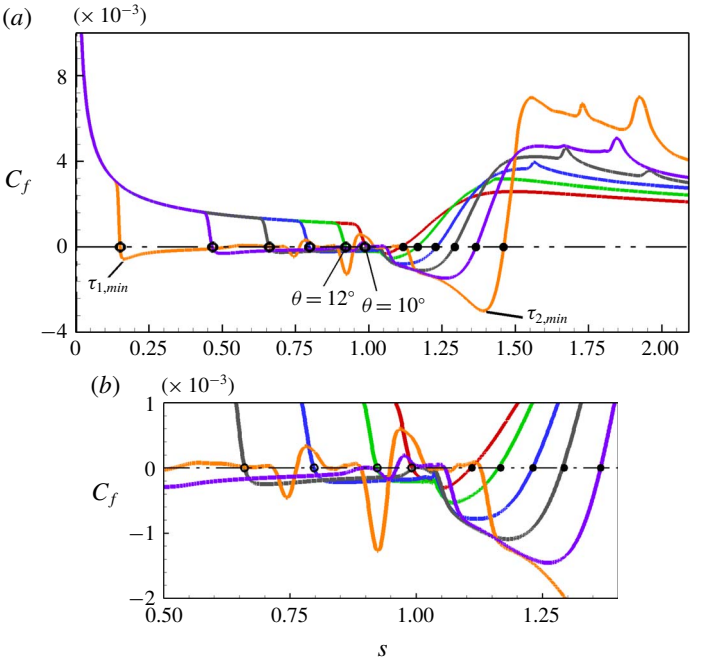


FIGURE 8. (Colour online) Variation of shear stress with deflection angle. Red: 10°; green: 12°; blue: 14°; grey: 16°; purple: 18°; orange: 24°. Open circles: separation; closed circles: reattachment. (*a*) Global distribution; (*b*) near the corner.

Another feature to note is that the rise to reattachment and peak pressure becomes steeper with increasing corner angle and so also the fall after reaching the peak.

Figure 8 shows the corresponding shear stress curves for these corner angles. They show the large changes occurring within the separated region with increasing deflection angle. After the near incipient separation with the 10° angle, the increase in separation length from 12° to 24° is more than fivefold. In this process, the separation point moves upstream and reattachment moves downstream. Multiple positive peaks with increasing corner angles are indicative of a number of secondary vortices. Another interesting feature is that at higher corner angles of 18° and 24° a 'knee' seems to appear on the front leg of the second minimum in shear stress corresponding to $\alpha = 4.47$ and $\alpha = 5.95$, respectively. Note also the steep rise in shear stress immediately after reaching the minimum and after reattachment (when the shear stress becomes positive) as the corner angle is increased.

Figures 9 and 10 respectively show global density gradients in the separated regions and in the corner region for all angles. In the figures the streamlines are superposed with major flow features annotated. These figures enable us to identify shock and compression waves at separation and reattachment, as well as vortices in the separated regions. Major features such as the leading edge shock (LES), separation shock (SS), reattachment shock (RS) and the triple point (TP) can all be identified. Secondly, at the 10° angle, we can see that separation (S) is about to develop. This is in agreement with the experimental result of Mallinson (1994), who found that the incipient separation angle was 10° ± 2°. Secondary vortices begin to appear at the 16° deflection angle at a corresponding scaled angle of $\alpha = 3.97$. At 18° and

https://doi.org/10.1017/jfm.2019.599 Published online by Cambridge University Press

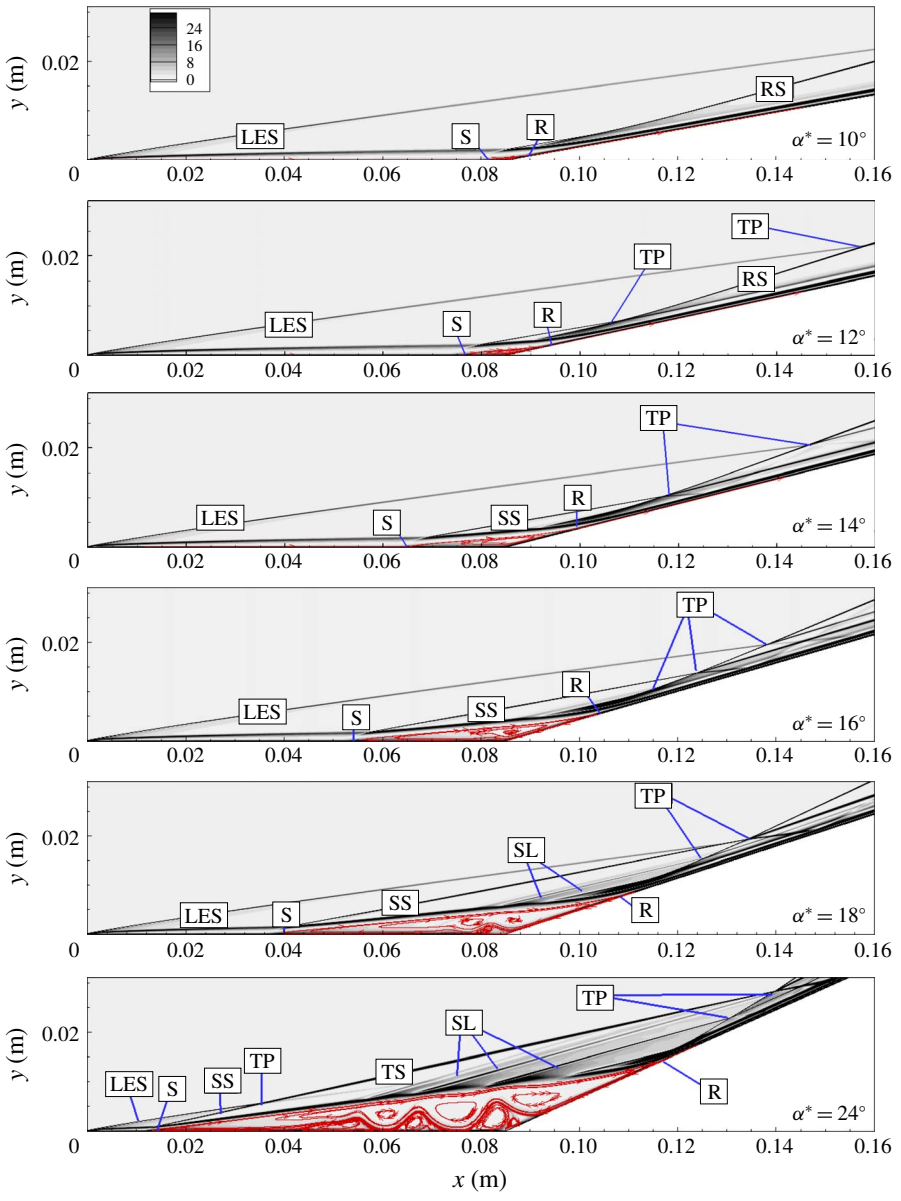


FIGURE 9. (Colour online) Density gradients (Kg m^{-4}) for the different deflection angles with streamlines superposed. LES, leading edge shock; SS, separation shock; TP, triple point; SL, shocklets; RS, recompression shock; TS, transmitted shock; S, separation; R, reattachment; DSL, dividing streamline.

24° corresponding to $\alpha = 4.47$ and 5.95, we can identify three and eight vortices respectively within the separated region. Note that in the large deflection angle 18°, the wall vortices (total of three) become fragmented as well. An interesting feature here is that, corresponding to the crest of these embedded vortices, compression waves (SL) seem to originate, which manifest themselves as peaks in the pressure curves seen in figure 7.

https://doi.org/10.1017/jfm.2019.599 Published online by Cambridge University Press

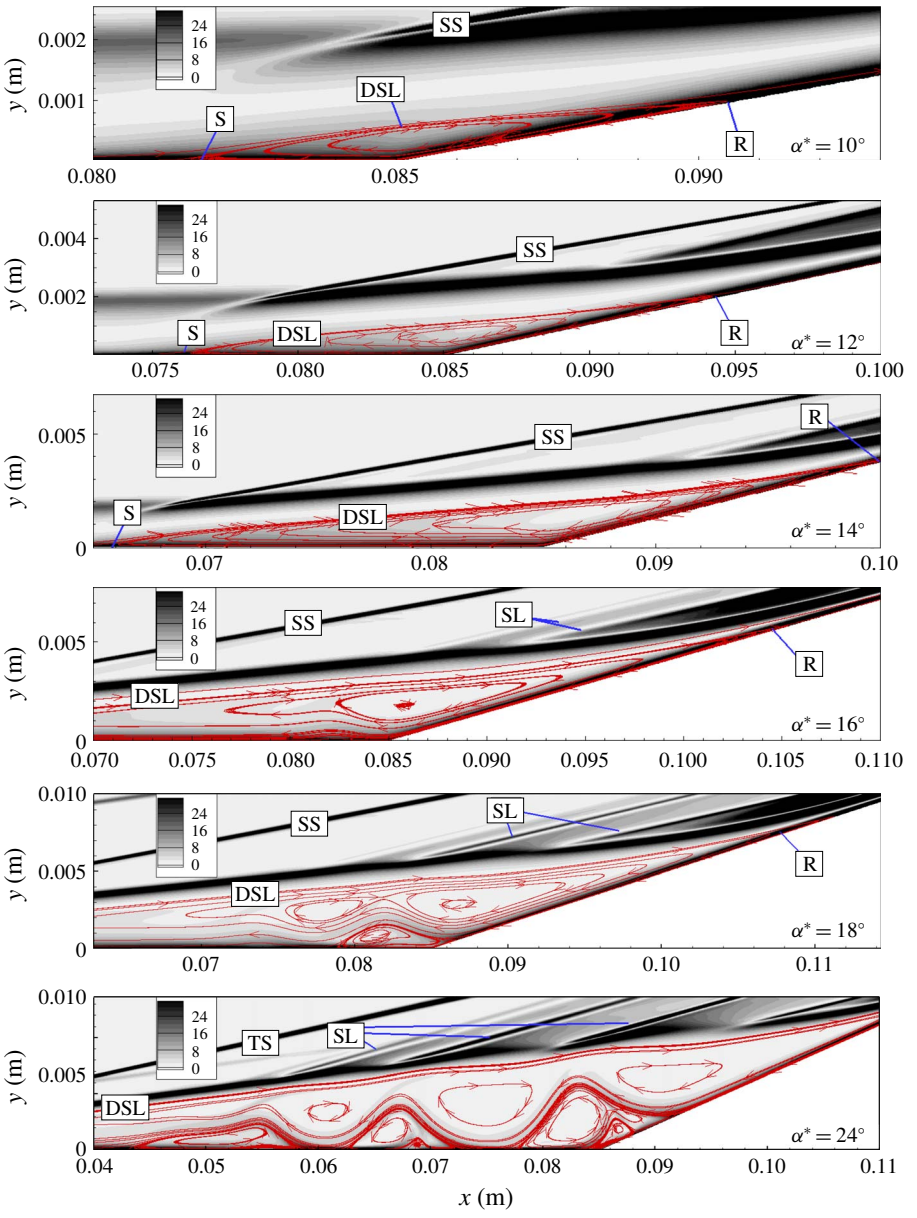


FIGURE 10. (Colour online) Density gradients (Kg m^{-4}) for the different deflection angles with streamlines superposed: corner region.

Figure 11 shows the vorticity distribution in the separated regions for all deflection angles. Section A-A' denotes the wall normal at the corner for angles 10°–14° and the reverse flow boundary layer as it separates for angles 16°–24°. We note small distortions (see sections A-A' to D-D' fore angles 16°–24° in the figure) begin to occur at 16° angle corresponding to $\alpha = 3.97$ and fragmentation into three secondary vortices has occurred at 18° with $\alpha = 4.47$. At the 24° corner angle with $\alpha = 5.95$ further fragmentation into eight secondary vortices has taken place.

https://doi.org/10.1017/jfm.2019.599 Published online by Cambridge University Press

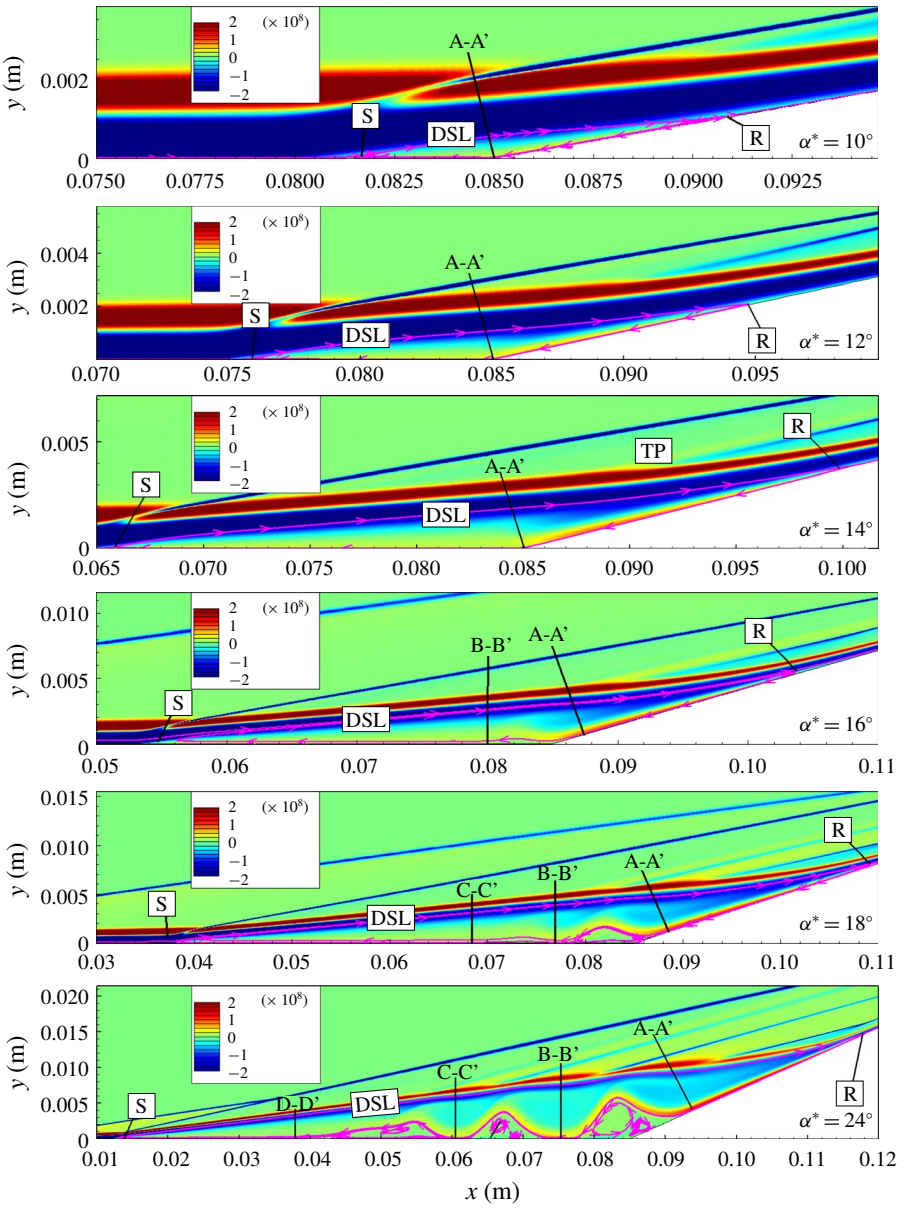


FIGURE 11. (Colour online) Vorticity ω_z contours (1 s^{-1}) for the different deflection angles with major streamlines superposed. A-A', wall normal at the reverse flow boundary layer or corner; B-B' to D-D', wall normals at each vortex.

These general flow features of large separated flows, namely, two shear stress minima, a distinct pressure plateau and multiple secondary vortices, are consistent with the studies by Smith & Khorrami (1991), Korolev *et al.* (2002) and Shvedchenko (2009) (see figures 4*a* and 4*b*). Our results also agree with Shvedchenko's observation that steady secondary separation first occurs when $3 \leqslant \alpha \leqslant 4$ and considerable fragmentation takes place when $\alpha > 4.5$.

https://doi.org/10.1017/jfm.2019.599 Published online by Cambridge University Press

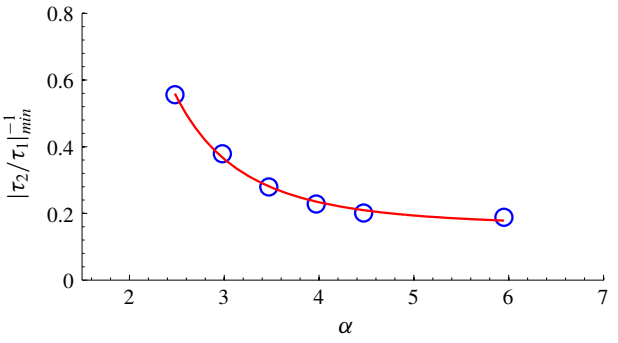


FIGURE 12. (Colour online) Variation of inverse of second minimum shear stress $|\tau_2/\tau_1|^{-1}_{min}$ with scaled angle α. Symbols denote data points.

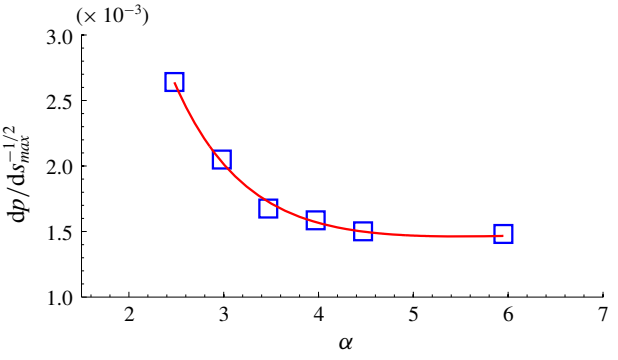


FIGURE 13. (Colour online) Variation of inverse pressure gradient $dp/ds^{-1/2}_{max}$ with scaled angle α. Symbols denote data points.

4.2. *Shear stress and pressure gradient in the reversed flow region*

Figures 12 and 13 show the variation of the second shear stress minimum $|\tau_2/\tau_1|^{-1}_{min}$ and the maximum pressure gradient at reattachment $dp/ds^{-1/2}_{max}$ with scaled angle α in the fashion of Smith & Khorrami (1991). The shear stress data in figure 12 show an increase in the magnitude of the minimum with increase in the scaled angle, and show virtually no significant change with $\alpha > 6$. Similarly, maximum pressure gradient values in figure 13 show an exponential decay to a near constant value for $\alpha > 6$. These changes in the magnitude of the second shear stress minimum and pressure gradient values with increase in the scaled angle for cold wall hypersonic separated flow are generally less severe than those in the Smith & Khorrami (1991) and Korolev *et al.* (2002) data because the Reynolds numbers in the present calculations are finite and moderate (of the order of 10^5) while the Smith & Khorrami (1991) and Korolev *et al.* (2002) solutions are asymptotically valid at large Reynolds numbers.

The rapid changes in the separated region and the appearance of the secondary separation and its fragmentation with the increase of scaled angle have their origin in the reverse flow boundary layer and its separation. This was first pointed out by Neiland (1970) and Stewartson (1975) and later discussed by Smith & Khorrami (1991), Neiland *et al.* (2008) and Shvedchenko (2009). The reverse flow boundary layer which develops in the reattachment region progressively encounters an adverse

https://doi.org/10.1017/jfm.2019.599 Published online by Cambridge University Press

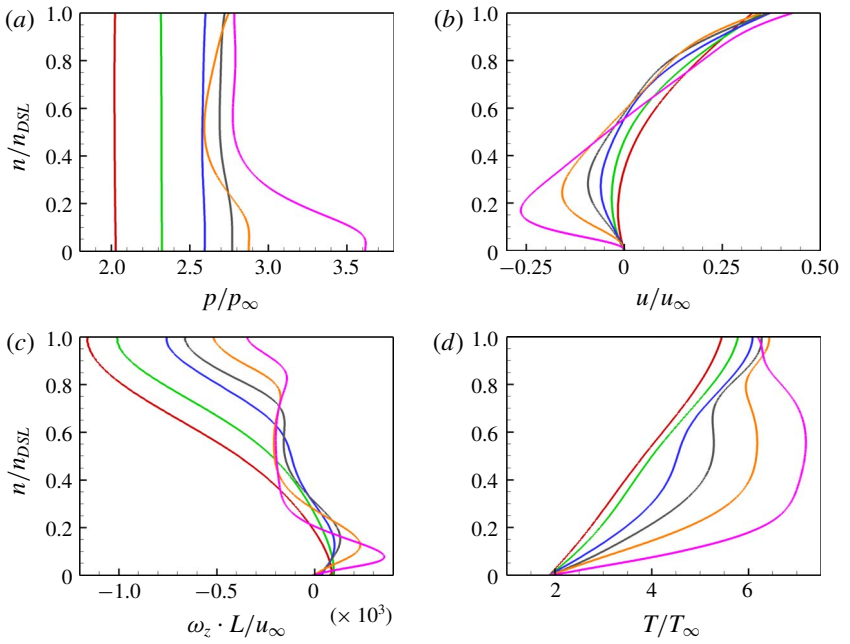


FIGURE 14. (Colour online) Reverse flow boundary layer (section A-A' in figure 11) profiles in all compression angles. Transverse distance n is normalised by the distance from the wall to the dividing streamline n_{DSL}. Red: 10°; green: 12°; blue: 14°; grey: 16°; orange: 18°; pink: 24°. (*a*) Pressure; (*b*) velocity; (*c*) vorticity; (*d*) temperature.

pressure gradient as it grows in the reverse direction and ultimately separates giving rise to secondary separations and vortices. This in turn creates transverse pressure gradients across the separated region. See also the discussion by Korolev (1991, 1992).

Figure 14 shows pressure (14*a*), velocity (14*b*), vorticity (14*c*) and temperature (14*d*) profiles for the reverse flow boundary layer region (see section A-A' in figure 11), where p, u and T are normalised by their corresponding free-stream values (subscript '∞'), while ω_z by u_∞/L, where L is length of the flat plate. The figure shows these properties for all compression angles 10°–24° corresponding to scaled angles $\alpha = 2.47$, 2.98, 3.47, 3.97, 4.47 and 5.95, respectively.

Considering pressure profiles first in figure 14(*a*), several features are noted. For angles up to 16°, the pressure across the separated region is constant and, as discussed previously, secondary separation has not yet occurred. At 18° angle ($\alpha = 3.97$), however, we see a small pressure gradient near the surface in the transverse direction and as seen in figure 10, secondary separation has occurred. With 24° angle ($\alpha = 5.95$), we see a strong transverse pressure gradient in the separated region near the surface and severe fragmentation into secondary vortices has occurred (figure 10).

Examination of the velocity profiles in figure 14(*b*) shows that with increasing angle, the primary separation size grows and when secondary separation begins to develop, we observe rapid variations in the reverse flow region near the surface and the profiles of 18° and 24° show inflection.

With regard to vorticity profiles in figure 14(*c*), up to 14°, initially, the vorticity is zero indicating separation and convects rapidly into the outer region showing one

https://doi.org/10.1017/jfm.2019.599 Published online by Cambridge University Press

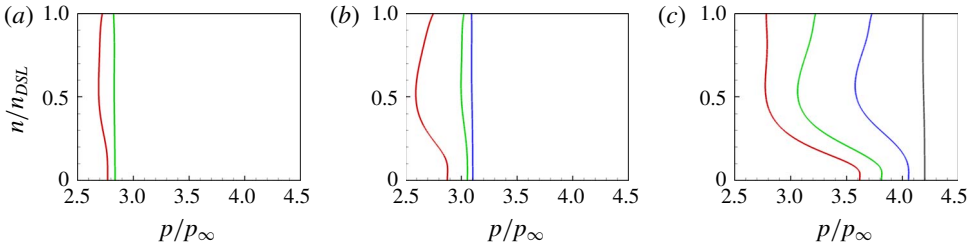


FIGURE 15. (Colour online) Pressure profiles at sections A-A' to D-D' (see figure 11) for angles 16°–24°. Transverse distance n is normalised by the distance from the wall to the dividing streamline n_{DSL}. Red: A-A'; green: B-B'; blue: C-C'; grey: D-D'. (*a*) 16°; (*b*) 18°; (*c*) 24°.

large eddy. With increase in the angle, secondary separation develops as seen from changes in slope of the profiles in the transverse direction. These changes in the transverse direction are accentuated as the secondary separation and the fragmentation into vortices take place. It is also seen that vorticity maxima become sharper and there are rapid variations in vorticity in the transverse direction with increasing α. Comparing the velocity and vorticity profiles in figures 14(*b*) and 14(*c*), it may be noted that vorticity maxima correspond to the inflection point in the corresponding velocity profiles.

Figure 14(*c*) shows temperature profiles. For each corner angle, the profiles indicate temperature through the main separated region and the vortices. Here for the lowest angle, there is a slight increase in temperature through the separated region but the temperature gradient at the surface shows no significant change for angles up to 16°. With the increase in the angle, and the presence of secondary vortices, not only wall temperature gradients increase but also regions of high temperature within the reverse flow show an increase.

Transverse pressures at sections A-A' to D-D' (see figure 11) are shown in figure 15 for angles 16° (15*a*), 18° (15*b*) and 24° (15*c*). They elaborate further on transverse gradients at different locations of the separated region. Pressure profiles at these sections show that gradients do exist before the separation of each vortex and increase with the increase in deflection angle. The profiles also show that the gradients decrease away from the reattachment region (A-A' to D-D').

4.3. *Further remarks on the shear stress minimum*

As discussed earlier, a significant feature of a large separated flow is the shear stress minimum immediately preceding reattachment. Secondly, this minimum is larger in magnitude than the one after separation. With increasing α, this minimum becomes steeper and sharper when the Reynolds number is very large as asymptotically valid solutions of Smith & Khorrami (1991) and Korolev *et al.* (2002) have shown. Smith (1988) and Smith & Khorrami (1991) suggested that when the scaled angle α is large enough, a stage may reach when $\tau_{2,min} \to -\infty$, a singularity. Subsequently, Korolev *et al.* (2002), based on Neiland's (1970) reattachment theory, found that their computations were smooth past the second minimum without encountering singularity for α up to 7.5. These findings were also confirmed by Logue, Gajjar & Ruban (2014).

To throw some light on this interesting feature of large separated flows, we have plotted the shear stress minimum τ_2 from available data in the literature, both

https://doi.org/10.1017/jfm.2019.599 Published online by Cambridge University Press

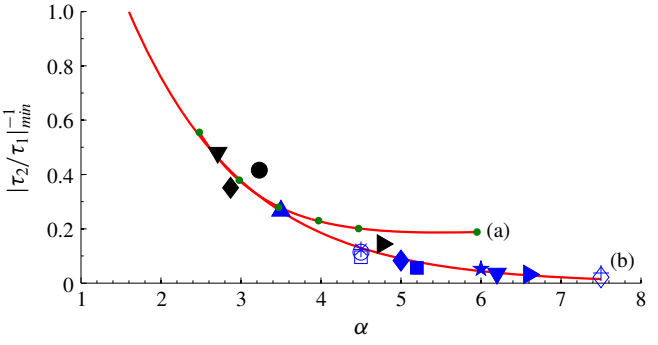


FIGURE 16. (Colour online) Variation of $|\tau_2/\tau_1|^{-1}_{min}$ with scaled angle α. Green dots in curve (a) present compression corner data for angles 10°–24° ($T_w/T_o = 0.125$). Curve (b) previous adiabatic wall data. (Black symbols: incident shock) ▼: Shrestha *et al.* (2016); ◆: Degrez, Boccadoro & Wendt (1987); ●: Katzer (1989); ►: Yao *et al.* (2007). (Blue symbols: compression corner) ▲, ○, ■, ▼ & ►: Smith & Khorrami (1991); □, ◆, ★ & ◇: Logue *et al.* (2014); ∗ & +: Korolev *et al.* (2002).

numerical and experimental, against the scaled angle α. It should be emphasised here that although some of these flows involved large separations (well-developed plateau), none discuss/comment on secondary separation or reverse boundary layer flow. As the various data (both compression corners and incident/ shock configuration) have been extracted directly from the quoted papers, some inaccuracies may likely have occurred and hence should be treated with caution. The trend, however, is quite clear.

Figure 16 shows the parameter $|\tau_2/\tau_1|^{-1}_{min}$ plotted against the scaled angle α. Apart from the present hypersonic cold wall data ($T_w/T_o = 0.125$), all other data are adiabatic and supersonic. The Reynolds numbers are generally of the order of 10^5 except those of the Smith & Khorrami (1991) and Korolev *et al.* (2002) data which are asymptotic solutions valid to $Re \to \infty$.

Considering the adiabatic wall data first, the trend from $\alpha = 2.5$ to 7.5 does show the second shear stress minimum $|\tau_2/\tau_1|^{-1}_{min}$ approaching zero for $\alpha \approx 8$. Smith & Khorrami (1994) have suggested a value 'somewhat below 9' for this critical value. These data are also consistent with the plateau appearing at $\alpha \geqslant 2.5$ indicating 'large' separated flow and a well-developed plateau (Burggraf 1975).

With respect to the present cold wall data, the first point to note is that the incipient separation angle is higher than the adiabatic value of 1.57. Secondly, with increasing α, the fall in the shear stress minimum is more gradual, reaching a near constant value for $\alpha \geqslant 6$. For a small wall temperature ratio ($T_w/T_o \leqslant 0.3$) and Reynolds number of the order of 10^5 Shvedchenko (2009) shows that steady secondary separations occur when α is between 5 and 6. He noted no secondary separation instabilities even at Reynolds number of the order of 10^6. His calculations do not extend beyond this value. This suggests that it is less likely that a critical value of α exists for low wall temperature ratios. Our previous study of wall temperature effects on leading edge separation (Khraibut *et al.* 2017; Khraibut 2018) are consistent with this view. Clearly, this is an area that needs further investigation.

4.4. *Size of the separation bubble*

Burggraf (1975) has shown that a large separated flow is characterised by $\alpha \geqslant 2.5$, and the bubble length scales as $\alpha^{3/2}$. Based on asymptotic theory, he proposed a relation

https://doi.org/10.1017/jfm.2019.599 Published online by Cambridge University Press

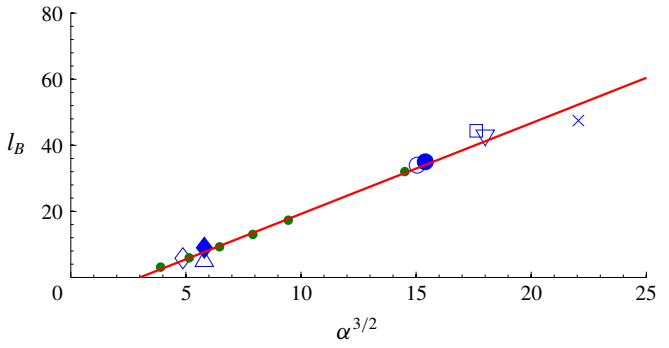


FIGURE 17. (Colour online) Variation of length of separation l_B with scaled angle α. Green dots: present compression corner data for angles 10°–24° ($T_w/T_o = 0.125$); ◇: Katzer (1989) (adiabatic); △: Degrez *et al.* (1987) (adiabatic); ◆: Rizzetta *et al.* (1978) (adiabatic); ○ & ●: Benay *et al.* (2006) ($T_w/T_o = 0.6$); □: Khraibut *et al.* (2017) ($T_w/T_o = 0.1$); ▽: Chapman *et al.* (1958) (adiabatic); ×: Swantek & Austin (2012) ($T_w/T_o \approx 0.04$).

for the plateau length L_p as

$$L_p = 3.47(\alpha - 1.55)^{3/2}, \tag{4.1}$$

which is valid for $\alpha \gg 1.55$.

It should be pointed out here that, although the actual length of the separation region is slightly different from the length of the pressure plateau, they have been used synonymously in the literature. For example, Korolev *et al.* (2002) assume $l_B \sim \alpha^{3/2}$, where l_B is the distance between separation and reattachment points. Rizzetta (1976) also assumes the same for compression corner separation. In actual fact, the bubble length comprises the plateau length and a reattachment region of $O(lRe^{-1/2})$ just after the end of the plateau and before reattachment (see Burggraf 1975 and Daniels 1979). In the present instance, we have taken the bubble length to vary as $\alpha^{3/2}$.

Burggraf (1975) also comments that there is a dearth of numerical solutions or experimental data to compare with his theoretical expression for separation bubble (plateau) length although he compares his theory with one of the Chapman *et al.* (1958) experimental results, which showed reasonable agreement. Figure 17 shows the bubble length l_B plotted against $\alpha^{3/2}$. The data correspond to compression corners, incident shock, leading edge separation and laminar axisymmetric SBLI. It is a linear relation with the zero intercept at $\alpha \approx 2.5$, which is when the plateau region develops. It shows that separation length is independent of the mode of generating large separations in line with the free-interaction concept. The data points shown here are estimated from the information provided from the quoted references, both numerical as well as experimental, and so may contain some inaccuracies but are believed adequate to draw conclusions. It is interesting to note this relationship seems also to be independent of wall temperature.

5. Conclusions

Large separated flows created with a flat plate compression corner geometry in hypersonic flow were investigated numerically and analysed. The characteristic features of large separated flows, a well-developed plateau region between separation

https://doi.org/10.1017/jfm.2019.599 Published online by Cambridge University Press

and reattachment and appearance of secondary separation at large enough scaled angle have been studied and verified in high Mach number/moderate Reynolds number hypersonic flow. The conditions when secondary separation first appears and when fragmentation into multiple vortices occurs are identified in terms of the scaled angle α and through detailed analysis of the reverse flow boundary layer and its separation.

Discussion of the second shear stress minimum and accompanying streamwise and transverse pressure gradients are discussed in the light of available (largely) supersonic adiabatic wall data and the present cold wall hypersonic data. While the available adiabatic wall data seem to indicate a critical scaled angle of approximately 8 as proposed by Smith (1988) for reversed flow singularity, the cold wall data did not show any tendency towards a critical angle.

It is shown that the size of the separated region is strongly dependent on the scaled angle being proportional to $\alpha^{3/2}$, in agreement with asymptotic expression of Burggraf (1975). It is also shown that this relationship is independent of the agency creating that separation. The relationship also appears to be independent of the wall temperature.

Acknowledgements

The authors are grateful to the Australian research Council for their support under grant DP-140100842. They would also like to thank National Computing Infrastructure (NCI) for providing computer resources. Sincere thanks are also due to Professor G. Candler of the University of Minnesota for permission to use the US3D code. The authors express their sincere thanks to the referees for their constructive comments and suggestions.

REFERENCES

Benay, R., Chanetz, B., Mangin, B., Vandomme, L. & Perraud, J. 2006 Shock wave/transitional boundary-layer interactions in hypersonic flow. *AIAA J.* **44** (6), 1243–1254.

Blottner, F. G., Johnson, M. & Ellis, M. 1971 Chemically reacting viscous flow program for multi-component gas mixtures. *Tech. Rep.* No. SC-RR-70-754. Sandia Labs.

Brown, S. N., Cheng, H. K. & Lee, C. J. 1990 Inviscid-viscous interaction on triple-deck scales in a hypersonic flow with strong wall cooling. *J. Fluid Mech.* **220**, 309–337.

Burggraf, O. R. 1975 Asymptotic theory of separation and reattachment of a laminar boundary layer on a compression ramp. *Tech. Rep.* AGARD-CP-168. AGARD.

Candler, G. V., Johnson, H. B., Nompelis, I., Gidzak, V. M., Subbareddy, P. K. & Barnhardt, M. 2015 Development of the US3D code for advanced compressible and reacting flow simulations. In *53rd AIAA Aerospace Sciences Meeting, AIAA Paper* 2015-1893. AIAA.

Candler, G. V., Subbareddy, P. K. & Brock, J. M. 2014 Advances in computational fluid dynamics methods for hypersonic flows. *J. Spacecr. Rockets* **52** (1), 17–28.

Chapman, D. R., Kuehn, D. M. & Larson, H. K. 1958 Investigation of separated flows in supersonic and subsonic streams with emphasis on the effect of transition. *NACA Tech. Rep.* 1356.

Cheng, H. K. 1993 Perspectives on hypersonic viscous flow research. *Annu. Rev. Fluid Mech.* **25**, 455–484.

Daniels, P. G. 1979 Laminar boundary-layer reattachment in supersonic flow. *J. Fluid Mech.* **90** (2), 289–303.

Deepak, N. R., Gai, S. L. & Neely, A. J. 2013 A computational investigation of laminar shock/wave boundary layer interactions. *Aeronaut. J.* **117** (1187), 27–56.

Degrez, G., Boccadoro, C. H. & Wendt, J. F. 1987 The interaction of an oblique shock wave with a laminar boundary layer revisited. An experimental and numerical study. *J. Fluid Mech.* **177**, 247–263.

https://doi.org/10.1017/jfm.2019.599 Published online by Cambridge University Press

DÉLERY, J. & MARVIN, J. G. 1986 Shock-wave boundary layer interactions. *Tech. Rep.* AGARDograph 280. AGARD.

DRAYNA, T. W., NOMPELIS, I. & CANDLER, G. V. 2006 Numerical simulation of the AEDC waverider at Mach 8. *AIAA Paper* 2005–2816.

DRUGUET, M. C., CANDLER, G. V. & NOMPELIS, I. 2005 Effects of numerics on Navier–Stokes computations of hypersonic double-cone flows. *AIAA J.* **43** (3), 616–623.

EGOROV, I., NEILAND, V. & SHVEDCHENKO, V. 2011 Three-dimensional flow structures at supersonic flow over the compression ramp. In *49th AIAA Aerospace Sciences Meeting including the New Horizons Forum and Aerospace Exposition*, p. 730. AIAA.

GITTLER, PH. & KLUWICK, A. 1987 Triple-deck solutions for supersonic flows past flared cylinders. *J. Fluid Mech.* **179**, 469–487.

HOLDEN, M. S. 1966 Experimental studies of separated flows at hypersonic speeds. II-two-dimensional wedge separated flow studies. *AIAA J.* **4** (5), 790–799.

HOLDEN, M. S., WADHAMS, T. P., HARVEY, J. K. & CANDLER, G. V. 2003 Comparisons between DSMC and Navier–Stokes solutions on measurements in regions of laminar shock wave/boundary layer interactions in hypersonic flows. *AIAA Paper* 2003-0435.

HUNG, C. M. & MACCORMACK, R. W. 1976 Numerical solutions of supersonic and hypersonic laminar compression corner flows. *AIAA J.* **14** (4), 475–481.

JACOBS, P. A. & GOLLAN, R. J. 2010 The Eilmer3 code. *Tech. Rep.* 2008/07. University of Queensland.

KATZER, E. 1989 On the lengthscales of laminar shock/boundary-layer interaction. *J. Fluid Mech.* **206**, 477–496.

KHRAIBUT, A. 2018 Laminar hypersonic leading edge separation. PhD thesis, University of New South Wales, Canberra.

KHRAIBUT, A., GAI, S. L., BROWN, L. M. & NEELY, A. J. 2017 Laminar hypersonic leading edge separation – a numerical study. *J. Fluid Mech.* **821**, 624–646.

KOROLEV, G. L. 1991 Asymptotic theory of laminar flow separation at a corner. *Fluid Dyn.* **26** (1), 150–152.

KOROLEV, G. L. 1992 Nonuniqueness of separated flow past nearly flat corners. *Fluid Dyn.* **27** (3), 442–444.

KOROLEV, G. L., GAJJAR, J. B. & RUBAN, A. I. 2002 Once again on the supersonic flow separation near a corner. *J. Fluid Mech.* **463**, 173–199.

LEWIS, J. E., KUBOTA, T. & LEES, L. 1968 Experimental investigation of supersonic laminar, two-dimensional boundary-layer separation in a compression corner with and without cooling. *AIAA J.* **6** (1), 7–14.

LOGUE, R. P., GAJJAR, J. & RUBAN, A. I. 2014 Instability of supersonic compression ramp flow. *Phil. Trans. R. Soc. Lond.* A **372** (2020), 20130342.

MACCORMACK, R. W. 2014 *Numerical Computation of Compressible and Viscous Flow*. AIAA.

MACLEAN, M. G., HOLDEN, M. S. & DUFRENE, A. T. 2014 Measurements of real gas effects on regions of laminar shock wave/boundary layer interactions in hypervelocity flows presented in AIAA Aviation 2014: Experimental Overview Paper. Available at: https://www.cubrc.org/_iassets/docs/laminar-xx-paper.pdf.

MALLINSON, S. G. 1994 Shock wave/boundary layer interaction at a compression corner in hypervelocity flows. PhD thesis, University of New South Wales, Canberra.

MALLINSON, S. G., GAI, S. L. & MUDFORD, N. R. 1997 The interaction of a shock wave with a laminar boundary layer at a compression corner in high-enthalpy flows including real gas effects. *J. Fluid Mech.* **342**, 1–35.

NEILAND, V. Y. 1970 Asymptotic theory of plane steady supersonic flows with separation zones. *Fluid Dyn.* **5** (3), 372–381.

NEILAND, V. Y., SOKOLOV, L. A. & SHVEDCHENKO, V. V. 2008 Temperature factor effect on the structure of the separated flow within a supersonic gas stream. *Fluid Dyn.* **43** (5), 706–717.

NOMPELIS, I. & CANDLER, G. V. 2014 US3D predictions of double-cone and hollow cylinder-flare flows at high enthalpy. *AIAA Paper* 2014-3366.

https://doi.org/10.1017/jfm.2019.599 Published online by Cambridge University Press

NOMPELIS, I., CANDLER, G. V. & HOLDEN, M. S. 2003 Effect of vibrational nonequilibrium on hypersonic double-cone experiments. *AIAA J.* **41** (11), 2162–2169.

OLEJNICZAK, J. & CANDLER, G. V. 1998 Computation of hypersonic shock interaction flow fields. In *7th AIAA/ASME Joint Thermophysics and Heat Transfer Conference, AIAA Paper* 1998-2446.

RIZZETTA, D. P. 1976 Asymptotic solution for two-dimensional viscous supersonic and hypersonic flows past compression and expansion corners. PhD thesis, Ohio State University, Columbus, OH.

RIZZETTA, D. P., BURGGRAF, O. R. & JENSON, R. 1978 Triple-deck solutions for viscous supersonic and hypersonic flow past corners. *J. Fluid Mech.* **89**, 535–552.

ROY, C. J. 2003 Grid convergence error analysis for mixed-order numerical schemes. *AIAA J.* **41** (4), 595–604.

RUDY, D., THOMAS, J., KUMAR, A., GNOFFO, P. A. & CHAKRAVARTHY, S. 1989 A validation study of four Navier–Stokes codes for high-speed flows. In *20th Fluid Dynamics, Plasma Dynamics and Lasers Conference, AIAA Paper* 1989-1838.

SHRESTHA, P., HILDEBRAND, N. J., DWIVEDI, A., NICHOLS, J. W., JOVANOVIC, M. R. & CANDLER, G. V. 2016 Interaction of an oblique shock with a transitional Mach 5.92 boundary layer. In *46th AIAA Fluid Dynamics Conference, AIAA Paper* 2016-3647.

SHVEDCHENKO, V. V. 2009 About the secondary separation at supersonic flow over a compression ramp. *TsAGI Sci. J.* **40** (5), 587–607.

SMITH, F. T. 1988 A reversed flow singularity in interacting boundary layers. *Proc. R. Soc. Lond.* A **A420**, 21–52.

SMITH, F. T. & KHORRAMI, A. F. 1991 The interactive breakdown in supersonic ramp flow. *J. Fluid Mech.* **224**, 197–215.

SMITH, F. T. & KHORRAMI, A. F. 1994 Hypersonic aerodynamics on thin bodies with interaction and upstream influence. *J. Fluid Mech.* **277**, 85–108.

STEWARTSON, K. 1970 On laminar boundary layers near corners. *Q. J. Mech. Appl. Maths* **23** (2), 137–152.

STEWARTSON, K. 1975 On the asymptotic theory of separated and unseparated fluid motions. *SIAM J. Appl. Maths* **28** (2), 501–518.

SWANTEK, A. B. & AUSTIN, J. M. 2012 Heat transfer on a double wedge geometry in hypervelocity air and nitrogen flows. In *50th AIAA Aerospace Sciences Meeting including the New Horizons Forum and Aerospace Exposition, AIAA Paper* 2012-0284.

TUMUKLU, O., LEVIN, D. A. & THEOFILIS, V. 2018 Investigation of unsteady, hypersonic, laminar separated flows over a double cone geometry using a kinetic approach. *Phys. Fluids* **30** (4), 046103.

VAN LEER, B. 1979 Towards the ultimate conservative difference scheme. V. A second-order sequel to Godunov's method. *J. Comput. Phys.* **32** (1), 101–136.

WILKE, C. R. 1950 A viscosity equation for gas mixtures. *J. Chem. Phys.* **18** (4), 517–519.

WRIGHT, M. J., CANDLER, G. V. & BOSE, D. 1998 Data parallel line relaxation method for the Navier–Stokes equations. *AIAA J.* **36** (9), 1603–1609.

YAO, Y., KRISHNAN, L., SANDHAM, N. D. & ROBERTS, G. T. 2007 The effect of Mach number on unstable disturbances in shock/boundary-layer interactions. *Phys. Fluids* **19** (5), 054104.

https://doi.org/10.1017/jfm.2019.599 Published online by Cambridge University Press